Labinot Topilla ✉
Serkan Toros

ANALYSIS OF THE FRACTURE BEHAVIOUR OF DUAL-PHASE STEELS USING THE GISSMO AND JOHNSON-COOK MODELS

Summary

This research explores an extended method of fracture mechanics to determine the parameters of the Johnson Cook and GISSMO models. The primary objective of the optimization process and iterative finite element method (FEM) was to identify optimised modelling parameters suitable for specimens with different shapes to predict the failure behaviour of dual-phase steels (DP), specifically DP600 and DP800 steels. Numerous experimental tests were conducted on these DP steels, which mainly consist of ferrite and martensite phases. The specimens underwent deformation at three different tensile velocities. To determine the flow curves, a Simplified Johnson-Cook model (MAT_SJC_098) was employed, while the Johnson-Cook model (MAT_JC_015) was used to identify failure, and a combined JC-GISSMO model was used to determine damage. The numerical simulation results were then compared with the experimental results. In conclusion, all modelling methods used in this research yielded the desired results.

Key words: dual phase, optimizations, numerical simulations. Johnson Cook, GISSMO

1. Introduction

Advanced high-strength steels (AHSS) are commonly used in the production of lightweight body-in-white (BIW) structures [1]. AHSS are a cost-effective solution with a high strength-to-weight ratio, superior formability, and excellent crashworthiness when compared to standard steels [2]. The combination of high strength and ductility makes AHSS a suitable material for manufacturing lightweight automobile components [3]. However, during stamping and forming operations, AHSS sheets may develop cracks at the cutting edges, as predicted by the formation of the limit diagram [4]. Quality control is therefore a very important process in this respect [5].

Dual-phase (DP) steels are advanced high-strength steels (AHSS) that have found widespread use in the automotive industry [6]. Developed in the late 1970s, DP steels are characterized by a microstructure consisting of ferrite and martensite phases [7]. As a new generation of high-strength steel, DP steels possess properties such as strength and formability [8]. These materials are often used in important safety components, as highlighted in [9], where the predictive failure of DP steel is compared to software simulations.

The specific mechanical properties of DP steels, such as high tensile strength, a high degree of hardening in the early stages of plastic deformation, and good ductility, are a result of their unique microstructure, which comprises ferrite and martensite phases. These properties set DP steels apart from high-strength low-alloy (HSLA) steels. In addition to these favourable features, DP steels exhibit good formability and ductility, which are important for their applications [10]. DP steels as ferritic-martensitic phase steels have a pronounced nonlinear unloading behaviour, which is subject to major changes and depends on the complex interaction of the sheet production process, resulting in a heterogeneous microstructure, as highlighted in [11].

An increase in the strength of DP steels can be achieved by increasing the volume fraction of martensite, which can be done by altering the carbon content or the intercritical annealing temperature, as noted by [12]. Compared to conventional low-carbon steels, DP steels have characteristic mechanical properties, such as low yield strength and high tensile strength, as stated by [13]. [1] conducted a study to investigate the damage mechanisms of DP1000 steel under various stress states and loading rates. The study showed that DP1000 steel exhibits more pronounced stress localization and a lower degree of damage during plastic deformation when compared to DP600 steel. The continuity of damage behaviour investigations in DP600 and DP800 steels was evaluated by [15] through standard uniaxial tensile testing, microstructural characterization, and finite element modelling. By determining the damage parameters of the Gurson-Tvergaard-Needleman (GTN) damage model and comparing the predicted outcomes with the experimental results, satisfactory agreement was achieved. This agreement facilitated an identification of the complete set of parameters for the GTN damage model specific to DP600 and DP800 steels.

Nowadays, computer simulations are contributing significantly to an understanding of materials behaviour, and even the behaviour of human bones [16], during stresses [17], deformations and failure. LS-DYNA is one software application used to study material behaviours, including models that determine cracking and failure. These models include the Gurson-Tvergaard-Needleman (GTN) damage model, micromechanics damage modelling (MDM), continuum damage mechanics (CDM) [18], and the Johnson-Cook model, etc. [19]. Additionally, a recent physical model called Hy-MFC has been developed to predict the mechanical properties of DP steels based on microstructural features such as chemical composition, martensite fraction, and grain size [20]. Several researchers have used the Johnson-Cook (JC) and Generalized Incremental Stress State Dependent Damage Model (GISSMO) models to investigate metal behaviour, and we will discuss some of their work in the following sections.

It is evident that the Johnson-Cook model has been extensively studied by various researchers in the field of materials science and engineering. The model's ability to predict the material's behaviour under different stress and temperature conditions has made it a popular choice in the industry. The determination of constitutive parameters such as A, B, n, and C for different materials is a crucial step in the model's implementation, as highlighted by [21]. Moreover, [22] and [23] have investigated the prediction of the model parameters under various stress and temperature conditions, while [2] has proposed an optimization approach to increase the model's predictability, taking into account strain rate hardening and thermal softening parameters. The JC model has also been applied to predict the ductility of Ti6Al4V titanium alloy sheets, as proposed by [25], where the model considers the effects of stress triaxiality, strain rate, temperature, and load parameters. The validation of the proposed model was done through tensile and shear performance tests, which showed promising results.

On the topic of material damage and failure prediction using the GISSMO model, extensive research has been conducted by [26], who compared the GISSMO and Damage

Initiation and Evolution Model DIEM models to predict material failure in LS-DYNA. Additionally, [27] verified the GISSMO characteristics for 980GEN3 steel by calibrating it with fracture testing in different deformation modes. They proposed an extended iterative FEM method to obtain GISSMO parameters. In another study, during the self-pierce riveting of thin aluminium sheets, the GISSMO damage model was used to describe the evolution of ductile damage and predict the onset of fracture, pre-damage, and material separation in the joining process simulation. The accuracy of crashworthiness capability simulations can be improved by using this model, as the results are comparable with good certainty. Therefore, the GISSMO damage model has shown promising results in predicting material separation, as reported by [28].

In this study, DP600 and DP800 steels underwent various mechanical property evaluation experiments. The obtained data were then used in several simulation studies, including the Johnson Cook model, where parameters such as A, B, n, C, and D1-D4 were calibrated. The GISSMO model was also utilized in a computer environment to assess the impact of materials on system performance.

In this study, the mechanical properties of DP600 and DP800 steel were evaluated through various experiments. The Simplified Johnson-Cook model (MAT_SJC_098) was used as the hardening/flow curve parameter model, and the Johnson-Cook model (Mat_0.15) and GISSMO damage/failure model available in LS-DYNA were used as the damage/failure model to calibrate the fracture behaviour of typical dual-phase steel. After the completion of the optimization and simulation processes, the results were validated through comparisons of the experimental and numerical data. The comparisons were based on stress-strain curves, effective plastic strains, and triaxiality factors, and their validity was assessed by relative error, where the results were in good agreement.

2. Materials and methods

2.1 Experimental methods

Two types of steel, DP600 and DP800, were prepared as materials for experimental testing in accordance with the ASTM E-8 standard [44]. These materials are widely used in the automotive industry due to their desirable properties, such as ease of use and low cost compared to other advanced high-strength steel (AHSS) types. Fig. 1 shows the four types of specimens that were tested, and their dimensions are presented in Tables 1 and 2. All uniaxial tensile tests were conducted using a Shimadzu Autograph 100 kN universal testing machine at three different tensile velocities: $v=25$ mm/min, $v=125$ mm/min, and $v=500$ mm/min. The elongation to final failure was measured by the video extensometer Digital Image Correlation (DIC) method, while the force results were measured by the tension loads exerted. All tests were conducted at constant room temperature based on the measurement method of [29]. Tables 1 and 2 present the experimental and numerical characteristics of specimens of the tested metals, as reported in [27]. These values are crucial in the simulation and optimisation process conducted in LS-OPT.
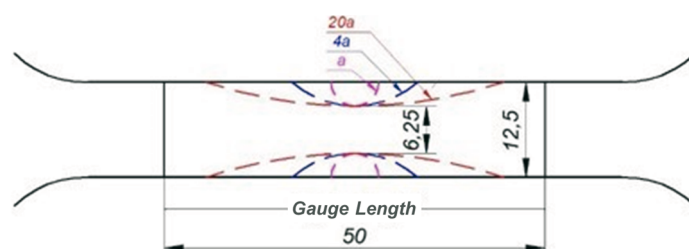

Fig. 1 Experimental smooth and notches tensile specimens.

Table 1 Summary of experimental and numerical specimen properties of DP600 steels. (a=3.125 mm)

Material BSL	Velocity EXP – SIM JC & GISSMO LS-OPT	Time Duration EXP s	Time Duration JC- GISSMO s	Thickness EXP SIM mm	Width EXP SIM mm	Gauge Length GL mm
DP600 - s	25 mm/min	35	42.5	0.77	12.5	50.4
DP600 - a		7.05	7.05	0.78	6.46	50.01
DP600 - 4a		7.07	7.07	0.77	6.35	50.46
DP600 - 20a		13.35	13.35	0.79	6.24	50.44
DP600 - s	125 mm/min	9.39	9.39	0.78	12.5	50.44
DP600 - a		1.3	1.3	0.78	6.49	50.27
DP600 - 4a		1.73	1.73	0.78	6.28	50.51
DP600 - 20a		2.44	2.44	0.79	6.32	50.24
DP600 - s	500 mm/min	2.14	2.16	0.78	12.52	50.51
DP600 - a		0.425	0.425	0.78	6.24	50.8
DP600 - 4a		0.41	0.41	0.78	6.25	50.48
DP600 - 20a		0.6	0.6	0.79	6.35	50.88

Table 2 Summary of experimental and numerical specimen properties of DP800 steels. (a=3.125 mm)

Material BSL	Velocity EXP – SIM JC & GISSMO LS-OPT	Time Duration EXP s	Time Duration JC- GISSMO s	Thickness EXP SIM mm	Width EXP SIM mm	Gauge Length GL mm
DP800 - s	25 mm/min	33	34.5	0.78	12.5	50.56
DP800 - a		8.35	8.35	0.76	6.2	51.03
DP800 - 4a		7.9	7.9	0.78	6.33	50.42
DP800 - 20a		8.65	8.65	0.78	6.36	50.64
DP800 - s	125 mm/min	7	7	0.77	12.56	50.68
DP800 - a		1.45	1.45	0.78	6.39	50.67
DP800 - 4a		3.43	3.43	0.77	6.23	50.7
DP800 - 20a		1.85	1.85	0.78	6.26	50.63
DP800 - s	500 mm/min	2.14	2.2	0.78	12.5	50.35
DP800 - a		0.38	0.38	0.78	6.4	50.4
DP800 - 4a		0.52	0.52	0.78	6.32	50.43
DP800 - 20a		0.88	0.88	0.78	6.42	50.37

2.1.1 Stress and strain curve calculations

After conducting the experimental tests, calculations were performed to optimize the process, simulate different scenarios, and compare the results. The calculations focused on engineering stress-strain, true stress-strain, and hardening curves. First, the engineering stress-strain curve was generated using a general equation (see Eqs. 1 and 2), which was then converted to a true stress-strain curve similar to that in [45] using other general equations (see Eqs. 3 and 4):

$$\sigma_{eng} = \frac{F}{A_0} \qquad \text{Engineering stress} \qquad (1)$$

$$\varepsilon_{eng} = \frac{l - l_0}{l_0} \qquad \text{Engineering strain} \qquad (2)$$

$$\varepsilon_{true} = \ln(1 + \varepsilon_{eng}) \qquad \text{True strain} \qquad (3)$$

$$\sigma_{true} = \sigma_{eng}(1 + \varepsilon_{eng}) \qquad \text{True stress} \qquad (4)$$

2.1.2   Discussion of experimental results

Fig. 2 (a, b, c, DP600, and d, e, f, DP800 steels) gives a graphical representation of the engineering stress-strain curves, derived from the experimental results. The smooth and notch specimens used in the experiment are named (s, 20a, 4a, and a), which are cut in the rolling direction (0°). The tensile test was performed at tensile velocity (*v)* of: *v*=25 mm/min, *v*=125 mm/min, and *v*=500 mm/min.
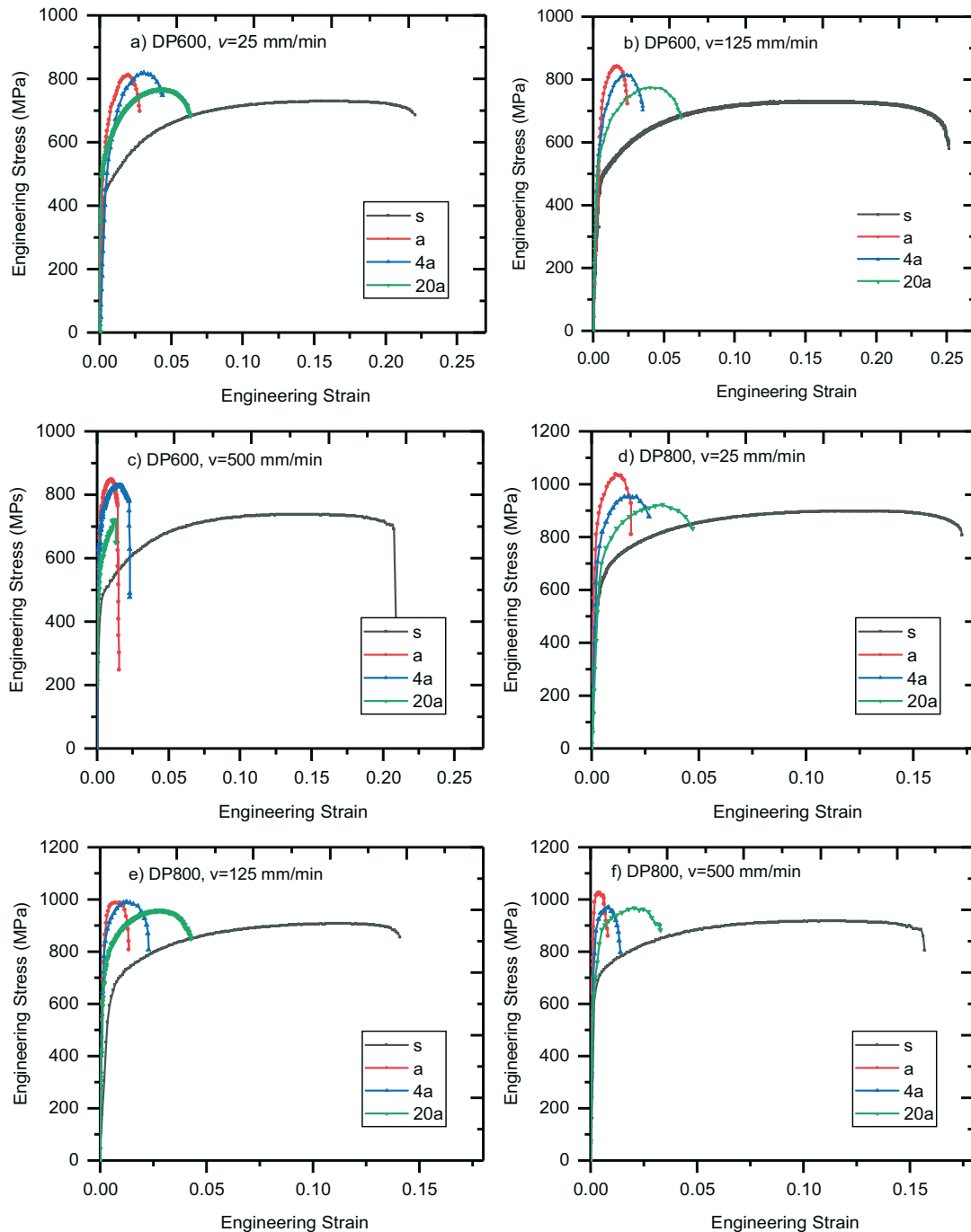

Fig. 2 Engineering stress-strain curves of DP600 and DP800 steels, tested at different tensile velocities.

Fig. 3 compares the tensile mechanical properties of DP600 and DP800 steels obtained experimentally, whose characteristics are described in Tables 1 and 2. The graphical representation shows the comparison between the engineering stress-strain results of the tested specimens at the tensile velocities mentioned earlier and for all points of interest. A detailed description of these points is displayed below.
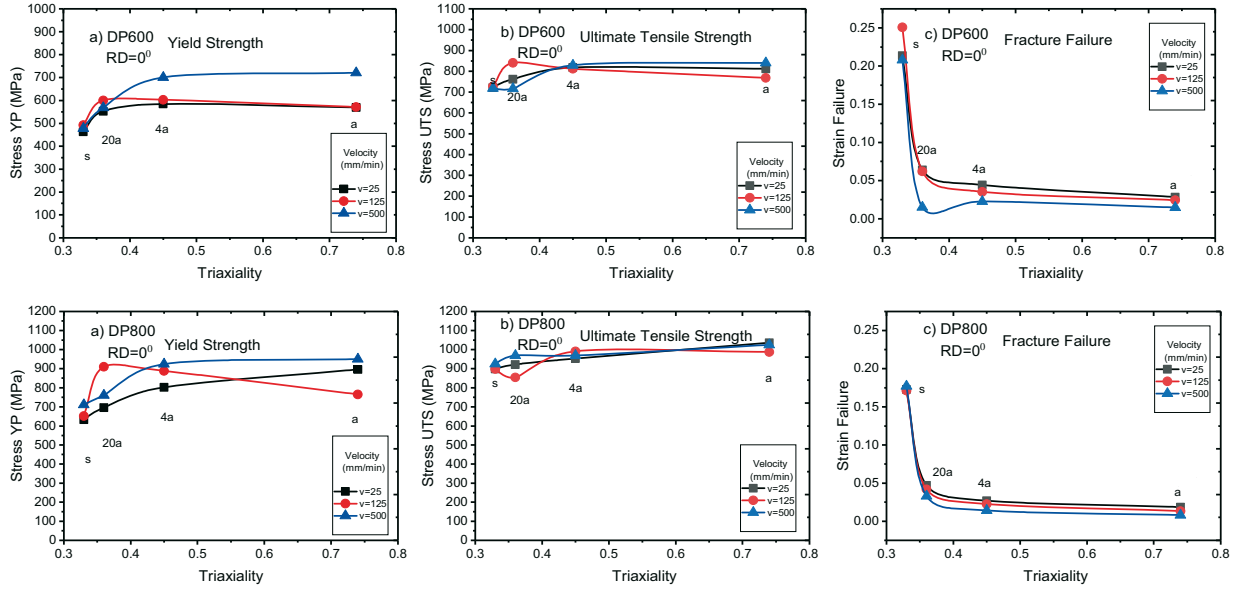
Fig. 3 Comparisons of the experimental results regarding yield strength (YP), ultimate tensile strength (UTS), and fracture failure (FF) of DP600 and DP800 steels tested at different tensile velocities.

Fig. 3 (a, d) expresses the comparisons of yield strength (YP) for the DP600 and DP800 steels of the tested specimens. The YP of the specimen (s) was significantly lower than the other specimens for both materials, while the YP of the other specimens (20a and a) had almost the same trajectory for both materials. The YP of the specimen (a) was higher than all other specimens for both materials at a tensile velocity of 500 mm/min. The experimental results suggest that the ultimate tensile strength (UTS) trajectory of specimens (s and a) is the same for both materials in all cases. However, for specimens (20a and 4a), the UTS trajectory was not similar in terms of testing velocity. For the DP600 steel specimen (20a), at a tensile velocity of 125 mm/min, it had a higher UTS compared to other specimens. On the other hand, for the DP800 steel specimens tested at a tensile velocity of 500 mm/min, the UTS was higher compared to other specimens. Fig. 3 (c) shows a comparison of elongation for the experimental measurements. The maximum elongation for both cases appears to be in specimen (s), while the minimum elongation for both cases appears to be in specimen (a).

2.1.3 Stress triaxiality

The stress triaxiality of four different geometrical shape specimens can be calculated using the equations below similar to [30]. Stress triaxiality is an important influential factor, where metal ductility decreases with increasing stress triaxiality [31]:

$$\eta = \frac{1}{3} + \ln\left(1 + \frac{a_0}{2R_0}\right) \tag{5}$$

a_0 - is the half of the total width of the narrowest region,

R_0 – is the notch radius.

The stress triaxiality is defined as the ratio of hydrostatic stress to von Mises equivalent stress

$$\eta = \frac{\sigma_h}{q} \tag{6}$$

$$\sigma_h = \frac{1}{3}(q1 + q2 + q3) \qquad \text{Hydrostatic stress} \tag{7}$$

$$q = \sqrt{\frac{(q1-q2)^2 + (q2-q3)^2 + (q1-q3)^2}{2}} \qquad \text{Mises equivalent stress [32].} \tag{8}$$

2.2 Finite element analysis and failure models

Finite element (FE) analysis was conducted using the LS-DYNA commercial finite element software [33] with the clear mechanical finisher. The FE models of the specimens were based on the ASTM E8 standard, and the tensile velocity and time duration used were similar to those of the experimental tensile test. The FE models were generated using the HyperMesh-LS-DYNA 971 Template Version, as shown in Fig. 4. The plastic flow curve was determined first in these FE analyses, followed by the determination of the fracture parameters and failure behaviours.

It is common to use different failure/damage models in studies, depending on the materials and their properties. In this study, the Simplified Johnson-Cook model was used to determine the flow curves, while the Johnson-Cook and JC-GISSMO models were used for failure/damage analysis. The Johnson Cook parameters can be determined by various methods, but in this study an optimization process was used to obtain the parameters that resulted in curves similar to the experimental ones. The aim was also to determine the tensile velocity that achieved results most similar to the experimental ones. The comparisons of the results obtained through LS-OPT for DP600 and DP800 steels are shown in Figs. 5 and 6, while Fig. 4 (a and b) shows the prepared specimens used for simulations.
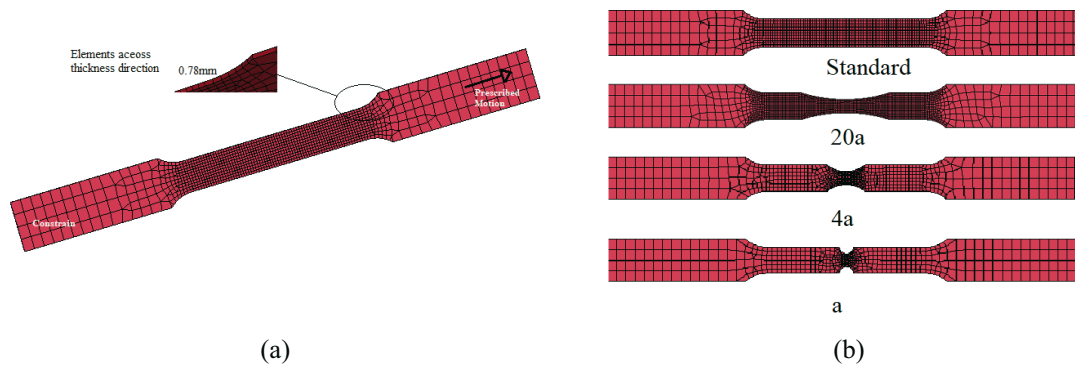

(a)　　　　　　　　　　　　　　　　　　　　(b)

Fig. 4 Numerical FEM model specimen used to define a) Simplified Johnson-Cook parameters,
b) Johnson-Cook parameters.

2.2.1 Simplified Johnson Cook model

Determination of the flow plastic curve was done using a simplified Johnson-Cook (MAT_SJC_098) model included in LS-DYNA for the examination of the above materials. Stress sensitivity J-C, material type 98, was used for difficulties when tensile velocities varied over a wide range. Thermal effects and damage were not taken into account in this updated model. This model is half as fast as the full J-C execution [34]. J-C expresses flow stress as:

$$\sigma_e = \left(A + B\bar{\varepsilon}^{p^n}\right)(1 + Cln\dot{\varepsilon}^*) \tag{9}$$

where A is the materials constant, B is the modulus of strain hardening, n is the exponent of strain hardening, and strain rate sensitivity index C, [35], σ_e is the Mises flow stress, $\bar{\varepsilon}^p$ is the equivalent plastic strain, and $\dot{\varepsilon}^* = \frac{\dot{\bar{\varepsilon}}}{ESPO}$ is the normalized effective strain rate. For the determination of the parameters A, B, n, and C, the optimization process was done through the LS-OPT software (see the results in Table 3). Optimized comparisons can be seen in Fig. 5.
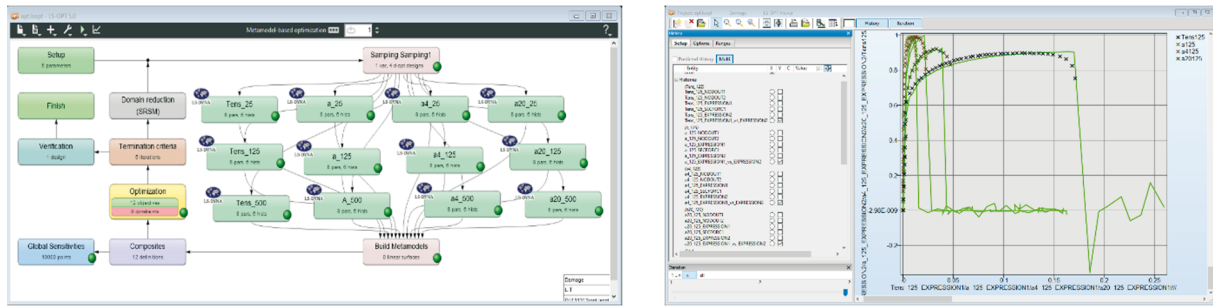
Fig. 5 Example of the process of optimizing and visually comparing the results
of the Simplified Johnson-Cook curves.

Table 3 Optimization results for the Simplified Johnson Cook model.

Mat	Velocity (mm/min)	A	B	n	C
DP600	v=25				
DP600	v=125	0.295	1.1	0.3515	0.00835
DP600	v=500				
DP800	v=25				
DP800	v=125	0.4451	1.2	0.3048	0.0136
DP800	v=500				

2.2.2 Johnson Cook damage/failure model

The constitutive relationship between Johnson and Cook (JC) is intended to characterize the material reaction under various stress conditions using a simple material model. Johnson developed the following relationship for failure and stress [36]. Johnson and Cook (1985) added a model for fracture based on cumulative damage to their basic model; this extra model feature is included in the LS-DYNA implementation of the Johnson-Cook model (Mat_0.15). The cumulative-damage fracture model entails the following equation: [37]

$$\varepsilon^f = max\left(\left[D_1 + D_2\, exp\, D_3\sigma^*\right]\left[1 + D_4 ln\, \dot{\bar{\varepsilon}}^*\right](1 + D_5 T^*), EFMIN\right), \qquad (10)$$

where $\sigma *$ is the ratio of pressure divided by effective stress, $\dot{\varepsilon}$ is the strain rate, and ε^f is the fracture strain. The constants *D1* through *D4* are material constants and are obtained from optimization, and T^* is the homologous temperature

$$\sigma^* = \frac{P}{\sigma_{eff}}\ . \qquad (11)$$

Fracture occurs when the damage parameter reaches the value of 1:

$$D = \sum \frac{\bar{\varepsilon}^p}{\varepsilon^f}\ . \qquad (12)$$

The variable D is stored as an extra history variable (4 in shell elements and 6 in solid elements), as indicated by reference [33]. Table 4 presents the parameters obtained from the optimizations performed for the Johnson-Cook model. Additionally, graphical comparisons using LS-OPT-history are shown in Fig. 6.

Fig. 6 Example of the process of optimizing and visually comparing the results of the Johnson-Cook curves.

Table 4 Optimization results for the Johnson-Cook model.

Mat	Velocity (mm/min)	D1	D2	D3	D4
DP600	v=25				
DP600	v=125	0.15371	0.10058	-2.9967	0.008
DP600	v=500				
DP800	v=25				
DP800	v=125	0.14284	0.31999	-9.5536	0.00354
DP800	v=500				

2.2.3 GISSMO model

The Generalized Incremental Stress State Dependent Damage Model (GISSMO) is a model developed to predict ductile damage based on incremental damage accumulation, including hardening and failure. This model was implemented in the finite element code LS-DYNA by [38]. The fracture strain limit curve, the equivalent plastic strain versus stress triaxiality, and the under plane stress state $\varepsilon^f(\eta)$ can be determined by several experiments [39].

Using this model, it is possible to define the properties and neck elongation values of materials with a certain load-bearing characteristic up to the point of fracture by analysing the constriction behaviour during shaping [40]. GISSMO is a damage accumulation rule that is explained and given by equations 13, 14, and 15 [41].

$$\Delta D = \frac{n}{\varepsilon^f} D^{(1-\frac{1}{n})} \dot{\varepsilon}_p. \tag{13}$$

If GISSMO is active, this equation is evaluated at any working time in LS-DYNA. The damage value D is accumulated in each element during deformation, and when the value of D reaches 1, it is considered that fracture has occurred. The values of triaxiality (η) and the increment of plastic strain ($\dot{\varepsilon}_p$) represent the equivalent failure strain, which allows for an arbitrary definition of triaxiality-dependent failure strains $\varepsilon^f(\eta)$ by inputting a tabulated curve.

A very useful aspect of GISSMO is the ability to accumulate a measure of instability, determined as:

$$\Delta F = \frac{n}{\varepsilon^c} F^{(1-\frac{1}{n})} \dot{\varepsilon}_p, \tag{14}$$

where ε^c is the triaxiality dependent critical strain $\varepsilon^c(\eta)$, while material instability noted by the letter F means that if $F = 0$ the material is undeformed, and if $F = 1$ it corresponds to the start of localization.

At the time when F reaches the effect, the element stress is reduced by

$$\sigma = \tilde{\sigma}\left[1 - \left(\frac{D - D_{crit}}{1 - D_{crit}}\right)^m\right], \tag{15}$$

where σ is the modified stress and $\tilde{\sigma}$ is the current stress. D_{crit} is the damage which only comes to some value when F reaches unity. The m is a fading exponent intended to better depict the rate of material hardening.

To define the flow curve, fracture parameters, and damage behaviours, the GISSMO model included in the ADD EROSION with the Johnson-Cook model is combined and functions together as a single body. Understandably, the ADD EROSION model includes failure and erosion options. The DEFINE velocity used in the key file for the GISSMO model was similar to that of the Johnson Cook model. The significance of velocity is also explained in the work of [42]. By combining these two models, the following main parameters are defined: fracture strain curve, ε^f, critical strain curve, ε^c, the fading exponent m *FADEXP,* which was set arbitrarily to 5 to achieve the fracture, while the damage exponent $n = 2$ *(DMGEXP)* was set based on [43], and equivalent plastic strain (*LCSDG*) was set for each case taken from previous Johnson Cook results. Figs. 10-11 show the comparative values of the Johnson-Cook and GISSMO models regarding effective plastic strain.

3. Results and discussion

3.1 Comparisons of experimental and numerical simulation results and validation

Fig. 7 (a, b, and c for DP600 and d, e, and f for DP800 steels) graphically compares the experimental and numerical results for engineering stress and strain. For both types of steel, the relative errors in fracture failure (FF) were less than 3% for the standard (s) specimens, while the relative errors were close to and up to 3% for other specimens named (20a) and more than the standard % for the named specimens (4a and a). For DP600 steel, the average relative errors for all standard specimens were about 1-3%, while for specimens (20a, 4a, and a), the average value of relative errors was higher than 3%. For DP800 steel, the average relative errors for all standard specimens were under 1%, while the average relative errors for specimens such as (20a, 4a, and a) were higher than 4%. It is important to note that all simulations were defined by the same parameters, and the best results were observed in standard (s) specimens, followed by specimens named (20a).
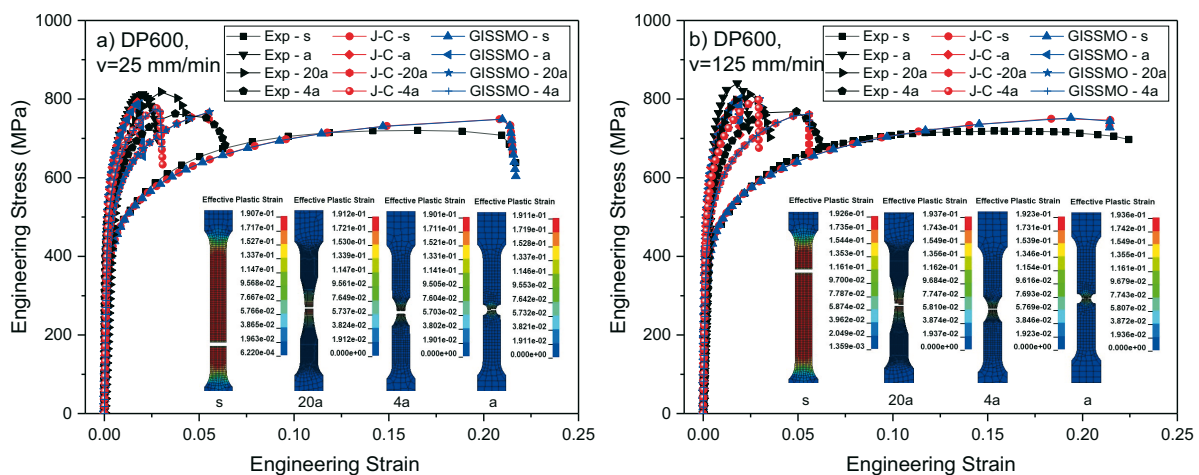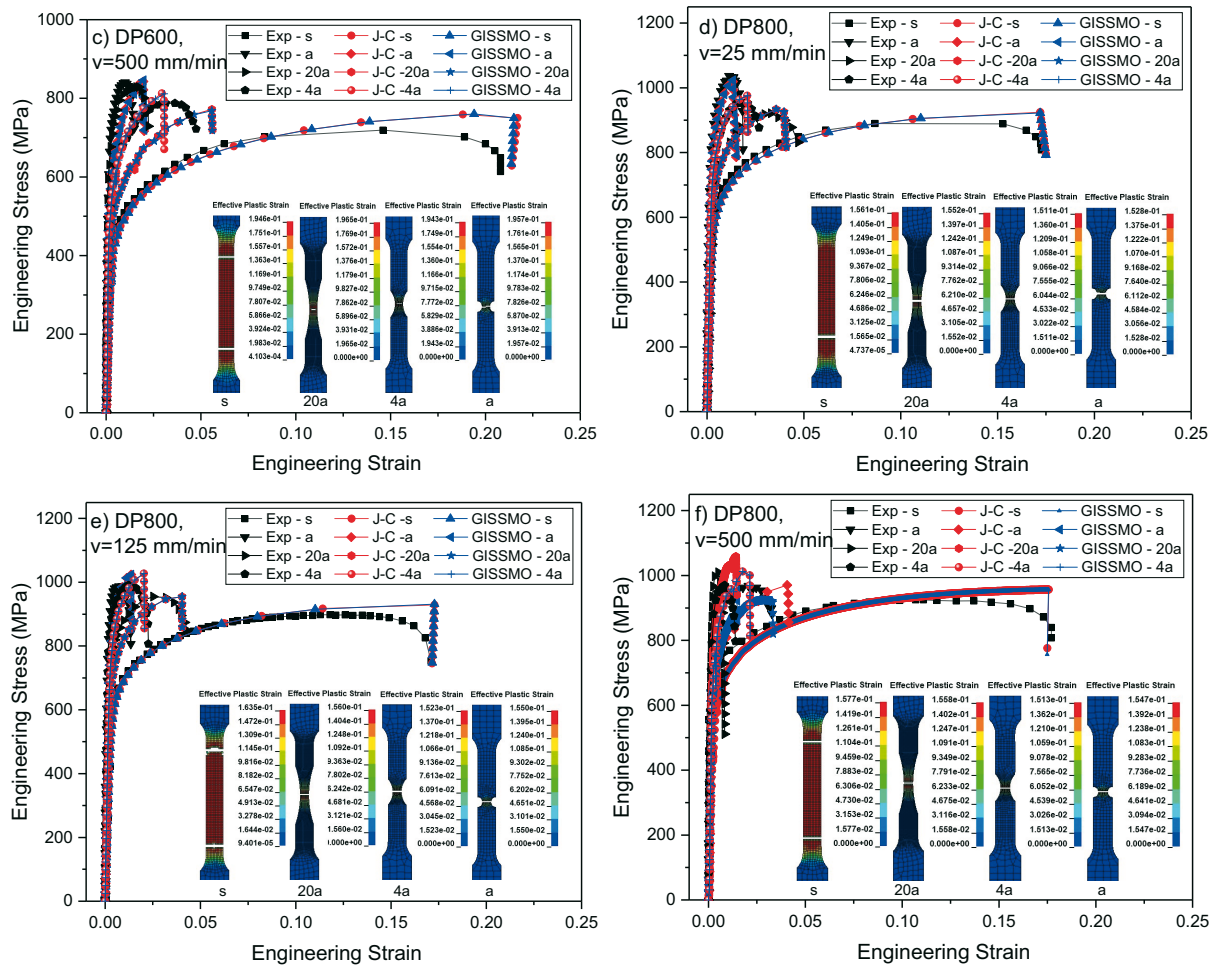
Fig. 7 Comparisons of experimental and numerical results regarding the engineering stress-strain curves of DP600 and DP800 steels tested at different tensile velocities.

Table 5 shows the relative errors in (YP), (UTS), and (FF) for each specimen separately. The numerical results are in good agreement with the experimental ones. Additionally, visual representations of the fractures of DP600 and DP800 steel samples obtained through the simulation are presented in Fig. 7.

The engineering force and displacement comparisons between the experimental and numerical results regarding DP600 and DP800 for certain points such as YP, UTS, and FF are presented in Figs. 8 and 9 in the (a-c) graphs.
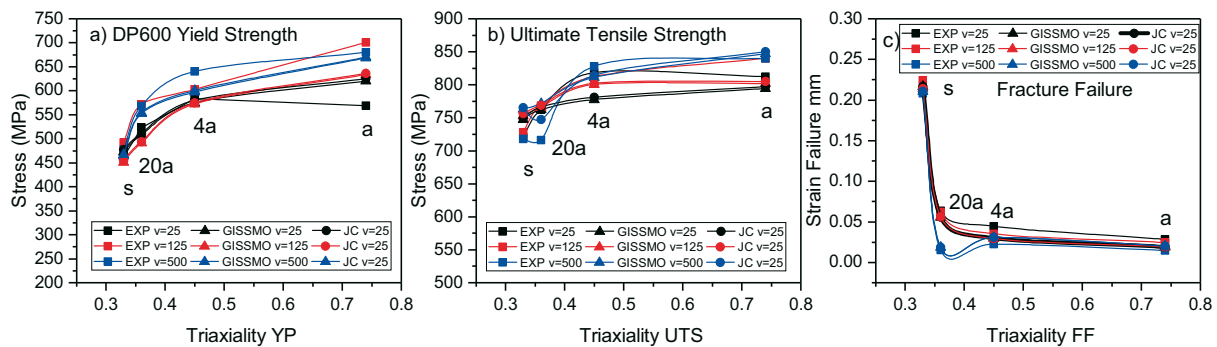
Fig. 8 Comparisons of experimental and numerical results regarding YP, UTS, and FF of DP600 steel tested at different tensile velocities.
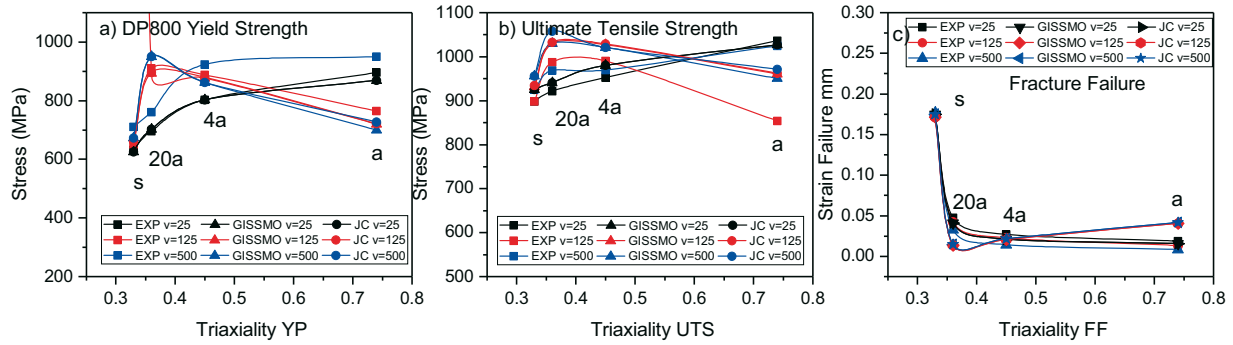
Fig. 9 Comparisons of experimental and numerical results regarding YP, UTS, and FF of DP800 steel tested at different tensile velocities.

The YP comparisons for all specimens are graphically shown in Figs. 8a and 9a where both types of metals can be visually compared. The most appropriate results were obtained at a tensile velocity of 25 mm/min, while the least desirable results were observed at a tensile velocity of 500 mm/min, as the tensile velocity had an effect. The UTS comparisons for both materials are presented in graphs (8b and 9b) for all cases. Based on the relative errors and graphics, it can be concluded that the most accurate results were obtained for the specimens where the displacement speed was 25 mm/min and 125 mm/min. Finally, the comparisons between the experimental and numerical measurements for fracture failure are shown in Figs. (8c and 9c). It can be concluded that the values achieved in all standard cases are within the standard of a fracture failure value below 3%, similar to [42], with a relative error standard between Δl (FEM) and Δl (Exp) below 3%.

3.2 Relative errors

This section presents the relative errors between the experimental results and the numerical results, which are presented in Table 5. Comparisons were made for all specimens tested, with a particular emphasis on tensile velocity, yield strength, ultimate tensile strength, and fracture failure. The relative errors were computed as:

$$error = \frac{(exp - num)}{num} x\ 100 \ . \tag{16}$$

In Eq. 16, "exp" represents the experimental results, while "num" represents the numerical results for all the points compared [46]. The results obtained are within the standard limit set by [27], which states that the standard deviation between experimental and numerical curves should be below 3% [27] and [42].

Table 5 Summary of relative errors (RE) between the experimental and numerical results for DP600 and DP800 steels.

Material	Tensile Velocity	RE YP	RE UTS	Engineering strain up to failure		
				Fracture Failure		
	Exp & Sim	Exp vs Sim	Exp vs Sim	Exp	Sim	R E (%)
DP600 - s	0.41666	-2.31%	-3.74%	0.21694	0.21666	0.13%
DP600 - s	2.08333	8.37%	-3.70%	0.22897	0.21412	2.94%
DP600 - s	8.33333	2.14%	-6.14%	0.208	0.21067	-1.27%
DP800 - s	0.41666	1.12%	-2.92%	0.17269	0.17504	-1.34%
DP800 - s	2.08333	-1.51%	-3.85%	0.171	0.17164	-0.37%
DP800 - s	8.33333	5.65%	-3.24%	0.177	0.17493	1.18%

Based on the data presented in Table 5, it is clear that the best results for all specimens and both types of steel were achieved when the tensile velocity was 25 mm/min for DP600 steel and 125 mm/min for DP800 steel.

3.3 Numerical effective plastic strain values

In the following section, numerical values of effective plastic strain (EPS) are presented for DP600 and DP800 steels, taking into consideration their different tensile velocities. Fig. 10 (a, b, and c DP600) and Fig. 11 (a, b, and c DP800) show the numerical effective plastic strain for all specimens analysed. In this case, a comparison was made between the JC model numerical results and the numerical results belonging to the GISSMO-JC model. The results were obtained directly from the software, specifically from the last value of EPS from all specimens.
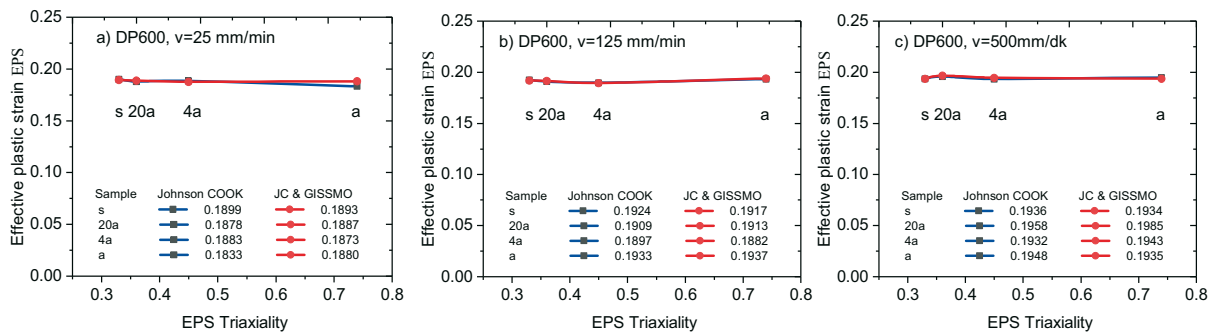
Fig. 10 Numerical data of the effective plastic strain of DP600 steel derived by the JC and GISSMO-JC models.
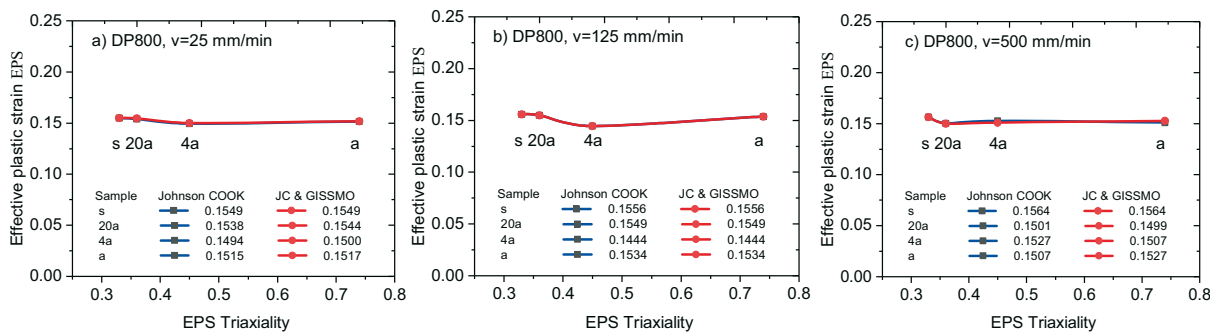
Fig. 11 Numerical data of the effective plastic strain of DP800 steel derived by the JC and GISSMO-JC models.

3.4 Numerical evolution of stress triaxiality

Fig. 12 (a, b, and c) presents the effective plastic strain vs. stress triaxiality for DP600 steel specimens with four different geometric shapes and tested at three different tensile velocities. Similarly, Fig. 13 (a, b, and c) shows the same comparison for DP800 steel. It is important to mention that stress triaxiality is an important influential factor, and metal ductility decreases with increasing stress triaxiality [31].

To investigate the impact of stress triaxiality on the specimen scale, shape, and tensile velocities of DP600 and DP800 steels in smooth and notch specimens, the development of stress triaxiality was determined and observed using the FEM results presented in Figs. 12–13.
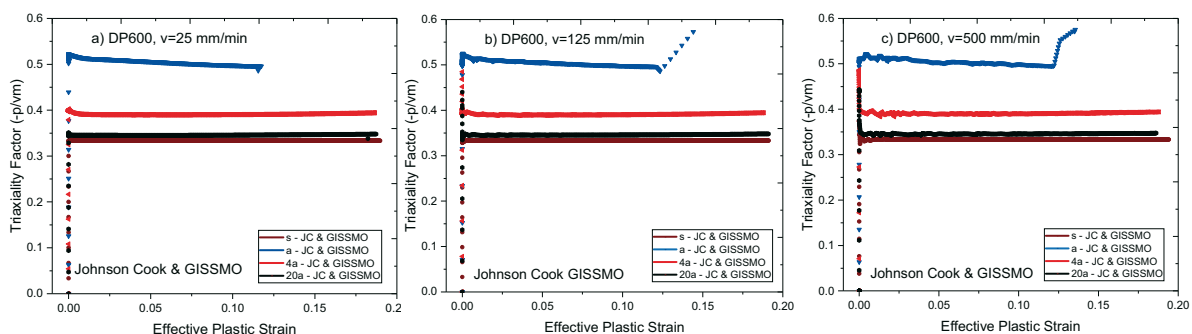
Fig. 12 Effective plastic strain and triaxiality curves for DP600 steel at different tensile velocities.
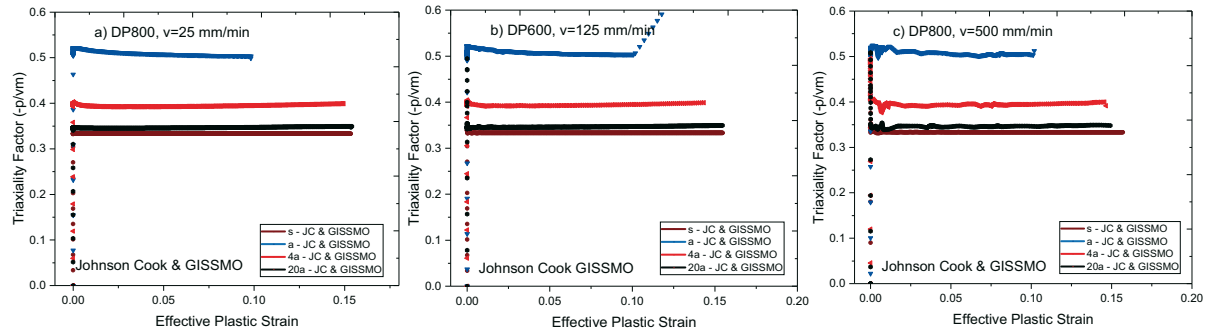
Fig. 13 Effective plastic strain and triaxiality curves for DP800 steel at different tensile velocities.

A point at the centre of each simulated specimen was selected to analyse the evolution of stress triaxiality with the displacement load. To compare the stress triaxiality in terms of specimen shape and tensile velocity, we divided them into three levels: an upper level with increasing stress triaxiality, a middle level with medium stress triaxiality, and a lower level with low stress triaxiality.

Based on Figs. 12–13, it is evident that an increase in the stress triaxiality factor results in a decrease in the ductility of the materials. Specimen (a) demonstrates the highest level of the triaxiality factor, indicating the greatest decrease in ductility. The middle level of the triaxiality factor is observed in specimens (4a and 20a), with specimen (4a) showing a higher triaxiality factor but with a shorter strain compared to specimen (20a), except for the comparison in Fig. 12 (c DP600). However, in Fig. 13 (b DP800), specimen 20a exhibits the highest ductility among all specimens at a tensile velocity of 125 mm/min. The standard (s) specimens exhibit the lowest level of the triaxiality factor but demonstrate the longest strain, as shown in Fig. 12 (a, b, and c DP600) and Fig. 13 (c DP800).

4. Conclusion

The paper describes both experimental and simulation methods used to predict fracture and failure of ductile steels. Through these methods, and by finding parameters, curves such as the stress-strain curve, flow curve, and effective plastic strain curve are determined, and the accuracy of these predictions is validated by comparing them with the experimental results.

From the two methods mentioned above, firstly the engineering and true stress-strain curves are defined, and then the parameters A, B, n, and C are defined from true plastic strain for both types of steel analysed at three different tensile velocities of 25 mm/min, 125 mm/min, and 500 mm/min. Subsequently, the failure parameters are defined.

To realize fractures, the JC model with the obtained parameters A, B, n, C, D1, D2, D3, and D4 is combined and functions together with GISSMO as a single mode. This interaction of models leads to the desired results. To achieve more believable results and a better fit of the curve, especially at fracture failure, it is important to note that the velocity set during the numerical simulations was the same as in the experimental cases.

The validation of the results was based on comparisons between the numerical and experimental results. Firstly, comparisons were made between the stress-strain curves, where almost all the results derived from the standard specimens were below 3% of relative errors, and the most accurate results were displayed in the sample named (s). Secondly, comparisons were made between the yield strength, ultimate tensile strength, and fracture failure, and Table 5 shows that the most accurate results in all cases appeared at fracture failure, which was the main objective. Finally, comparisons were made regarding the effective plastic strain and triaxiality factor, and, even in this case, very similar results appeared. In previous studies, we investigated the crack propagation of standard specimens and of microstructures using finite

element modelling [47] [48]. However, in this study, the J-C hardening and failure parameters are already determined, as are the GISSMO damage parameters. Additionally, the plan is to simulate the damages/failure on 3D microstructures via finite element modelling.

REFERENCES

[1]   Ren S, Ma N, Tsutsumi S, Watanabe G, He H, Cao C, Huang L. Post-weld cold working for fatigue strength improvement of resistance spot welded joint of advanced high-strength steel. Journal of Materials Processing Technology. 2022 Jan 1:1–11. https://doi.org/10.1016/j.jmatprotec.2021.117364

[2]   Kuziak R, Kawalla R, Waengler S. Advanced high strength steels for automotive industry. Archives of civil and mechanical engineering. 2008;8(2):103-117. https://doi.org/10.1016/S1644-9665(12)60197-6

[3]   Shojaee M, Midawi AR, Barber B, Ghassemi-Armaki H, Worswick M, Biro E. Mechanical properties and failure behavior of resistance spot welded third-generation advanced high strength steels. Journal of Manufacturing Processes. 2021 May 1;65:364-372. https://doi.org/10.1016/j.jmapro.2021.03.047

[4]   Terrazas OR, Findley KO, Van Tyne CJ. Influence of martensite morphology on sheared-edge formability of dual-phase steels. ISIJ International. 2017 May 15;57(5):937-944. https://doi.org/10.2355/isijinternational.ISIJINT-2016-602

[5]   Janjić G, Tanasić Z, Tomić Stojković R. Development of a quality management model in the automotive industry with a focus on the quality of incoming products (Part I). Transactions of FAMENA. 2022 Apr 29;46(1):115-126. https://doi.org/10.21278/TOF.461030921

[6]   Ozturk F, Toros S, Kilic S. Effects of anisotropic yield functions on prediction of forming limit diagrams of DP600 advanced high strength steel. Procedia Engineering. 2014 Jan 1;81:760-765. https://doi.org/10.1016/j.proeng.2014.10.073

[7]   Kulakov M, Poole WJ, Militzer M. A microstructure evolution model for intercritical annealing of a low-carbon dual-phase steel. ISIJ International. 2014 Nov 15;54(11):2627-2636. https://doi.org/10.2355/isijinternational.54.2627

[8]   Çavuşoğlu O, Toros S, Gürün H, Güral A. Warm deformation and fracture behaviour of DP1000 advanced high strength steel. Ironmaking & Steelmaking. 2018 Aug 9;45(7):618-625. https://doi.org/10.1080/03019233.2017.1309168

[9]   Andrade F, Feucht M. A comparison of damage and failure models for the failure prediction of dual-phase steels. n 11th European LS-DYNA Conference. Salzburg, Austria. 2017.

[10]   Bello KA, Hassan SB, Aponbiede O. Effects of austenitising conditions on the microstructures and mechanical properties of martensitic steel with dual matrix structure. Journal of Minerals & Materials Characterization & Engineering. 2011;11(1):69-83. https://doi.org/10.4236/jmmce.2012.111006

[11]   Robl T, Krempaszky C, Fillafer A, Werner E. Examining the unloading behavior of dual-phase steels by means of microstructure simulations. Materials Science and Engineering: A. 2021 Aug.: 1–9. https://doi.org/10.1016/j.msea.2021.141744

[12]   Matlock DK, Speer JG. Third generation of AHSS: microstructure design concepts. In Microstructure and Texture in Steels: and Other Materials 2009 (pp. 185-205). https://doi.org/10.1007/978-1-84882-454-6_11

[13]   Sodjit S, Uthaisangsuk V. A micromechanical flow curve model for dual phase steels. Journal of Metals, Materials and Minerals. 2012 Jun 30;22(1).: 87–97

[14]   Liu W, Lian J, Münstermann S. Damage mechanism analysis of a high-strength dual-phase steel sheet with optimized fracture samples for various stress states and loading rates. Engineering Failure Analysis. 2019 Dec: 1–23. https://doi.org/10.1016/j.engfailanal.2019.08.004

[15]   Santos RO, Da Silveira LB, Moreira LP, Cardoso MC, Da Silva FRF, Dos Santos Paula A, et al. Damage identification parameters of dual-phase 600-800 steels based on experimental void analysis and finite element simulations. J Mater Res Technol. 2019;8(1):644–659. https://doi.org/10.1016/j.jmrt.2018.04.017

[16]   Verim Ö. Development and investigation of the mechanical behaviour of circular external fixators during the gait cycle. Transactions of FAMENA. 2022 Apr 29;46(1):81-90. https://doi.org/10.21278/TOF.461029121

[17]   Gao H, Fan Q, Chu Z. Simulation research on the forming process of large axles rolled by cross-wedge rolling. Transactions of FAMENA. 2022 Sep 18;46(3):63-80. https://doi.org/10.21278/TOF.463043422

[18]   Chalal H, Abed-Meraim F. Determination of forming limit diagrams based on ductile damage models and necking criteria. Lat Am J Solids Struct, 2017;14(10): 1872–1892. https://doi.org/10.1590/1679-78253481

[19] Wang Z, Hu Z, Liu K, Chen G. Application of a material model based on the Johnson-Cook and Gurson-Tvergaard-Needleman model in ship collision and grounding simulations. Ocean Engineering. 2020 Jun: 1–12. https://doi.org/10.1016/j.oceaneng.2019.106768

[20] Mathevon A, Fabrègue D, Massardier V, Cazottes S, Rocabois P, Perez M. Investigation and mean-field modelling of microstructural mechanisms driving the tensile properties of dual-phase steels. Materials Science and Engineering: A. 2021 Aug: 1–12. https://doi.org/10.1016/j.msea.2021.141532

[21] Karkalos NE, Markopoulos AP. Determination of Johnson-Cook material model parameters by an optimization approach using the fireworks algorithm. Procedia Manufacturing. 2018 Jan 1;22:107-113. https://doi.org/10.1016/j.promfg.2018.03.017

[22] Grzesik W, Niesłony P, Laskowski P. Determination of Material Constitutive Laws for Inconel 718 Superalloy Under Different Strain Rates and Working Temperatures. J Mater Eng Perform. 2017;26(12): 5705–5714. https://doi.org/10.1007/s11665-017-3017-8

[23] Yu SS, Lu Y Bin, Cai Y. The strain-rate effect of engineering materials and its unified model. Lat Am J Solids Struct. 2013;10(4): 833–844. https://doi.org/10.1590/S1679-78252013000400010

[24] Murugesan M, Jung DW. Johnson Cook material and failure model parameters estimation of AISI-1045 medium carbon steel for metal forming applications. Materials. 2019 Feb 18;12(4):609: 1–18. https://doi.org/10.3390/ma12040609

[25] Valoppi B, Bruschi S, Ghiotti A, Shivpuri R. Johnson-Cook based criterion incorporating stress triaxiality and deviatoric effect for predicting elevated temperature ductility of titanium alloy sheets. International Journal of Mechanical Sciences. 2017 Apr 1;123:94-105. https://doi.org/10.1016/j.ijmecsci.2017.02.005

[26] Anderson D, Butcher C, Pathak N, Worswick MJ. Failure parameter identification and validation for a dual-phase 780 steel sheet. Int J Solids Struct. 2017;124:89–107. http://dx.doi.org/10.1016/j.ijsolstr.2017.06.018

[27] Xiao Y, Hu Y. An extended iterative identification method for the GISSMO model. Metals (Basel). 2019;9(5).569: 1–16. https://doi.org/10.3390/met9050568

[28] Otroshi M, Rossel M, Meschut G. Stress state dependent damage modeling of self-pierce riveting process simulation using GISSMO damage model. Journal of Advanced Joining Processes. 2020 Mar 1;1: 1–8. https://doi.org/10.1016/j.jajp.2020.100015

[29] Toros S, Ozturk F. Modeling uniaxial, temperature and strain rate dependent behavior of Al-Mg alloys. Comput Mater Sci. 2010 Aug 1;49(2):333–339. https://doi.org/10.1016/j.commatsci.2010.05.019

[30] Bridgman PW. Studies in large plastic flow and fracture: with special emphasis on the effects of hydrostatic pressure. Harvard University Press; 1964 Dec 31. https://doi.org/10.4159/harvard.9780674731349

[31] Brünig M, Chyra O, Albrecht D, Driemeier L, Alves M. A ductile damage criterion at various stress triaxialities. International journal of plasticity. 2008 Oct 1;24(10):1731-55. https://doi.org/10.1016/j.ijplas.2007.12.001

[32] Peng J, Wang Y, Dai Q, Liu X, Liu L, Zhang Z. Effect of stress triaxiality on plastic damage evolution and failure mode for 316L notched specimen. Metals. 2019 Sep 30;9(10):1067: 1–17. https://doi.org/10.3390/met9101067

[33] Ls-Dyna ® keyword user's manual volume ii material models livermore software technology corporation (lstc) [Internet]. 2012. Available from: www.lstc.com

[34] Stander N, Roux W, Goel T, Eggleston T, Craig Ken. ls-opt User's Manual: A design optimization and probabilistic analysis tool. Technology. 2012.

[35] Stopel M, Skibicki D. Determination of Johnson-Cook model constants by measurement of strain rate by optical method. AIP Conf Proc. 2016 (October);1780: 060003-9. https://doi.org/10.1063/1.4965956

[36] Johnson GR, Cook WH. A constitutive model and data from metals subjected to large strains, high strain rates and high temperatures. In: Proc 7th {I}nt {S}ymp on {B}allistics, {T}he {H}ague, {N}etherlands. 1983.

[37] Schwer L. Optional Strain-rate forms for the Johnson Cook Constitutive Model and the Role of the parameter Epsilon_0. In6th European LS_DYNA Users' conference 2007 May 29 (pp. 1-17).

[38] Pérez Caro L. Modelling of Forming and Welding in Alloy 718." PhD diss., Luleå University of Technology, 2017.

[39] Chen X, Chen G, Huang L. Validation of GISSMO model for fracture prediction of a third-generation advanced high-strength steel. SAE International Journal of Materials and Manufacturing. 2018 Jan 1;11(4):293-302. https://doi.org/10.4271/2018-01-0107

[40]   P. Du Bois and M. Feucht, "Increasing predictability in crashworthiness simulation: pushing the limits,"
        Ger. LS-DYNA Forum, 2012.

[41]   Andrade F (Daimler A, Feucht M (Daimler A, Haufe A (DYNAmore G. On the Prediction of Material
        Failure in LS-DYNA ® : A Comparison Between GISSMO and DIEM. 13th Int LS-DYNA Users Conf.
        2014:1–12.

[42]   Xiao Y, Tang Q, Hu Y, Peng J, Luo W. Flow and fracture study for ZK60 alloy at dynamic strain rates
        and different loading states. Materials Science and Engineering: A. 2018 May 2;724:208-219.
        https://doi.org/10.1016/j.msea.2018.03.050

[43]   Basaran M, Wölkerling SD, Feucht M, Weichert D, Ag D. An Extension of the GISSMO Damage Model
        Based on Lode Angle Dependence. LS-DYNA Anwenderforum. 2010 Oct;15:15

[44]   Devanathan C, SureshBabu A. Multi objective optimization of process parameters by firefly algorithm
        during the friction stir welding of metal matrix composites. Transactions of FAMENA. 2021 May
        19;45(1):117-128. https://doi.org/10.21278/TOF.451018520

[45]   Ali KB, Demir B, Gürün H, Acarer M. Influence of punch shapes on forces and part quality in the
        punching of explosively welded DP600, Al1100, and DP600-Al1100 composite plates. Transactions of
        FAMENA. 2022 Jun 15;46(2):55-68. https://doi.org/10.21278/TOF.462039222

[46]   de Oliveira SMF, Sousa LL de C, Vidal CA, Cavalcante-Neto JB. A locally-continuous meshless local
        petrov-galerkin method applied to a two-point boundary value problem. Lat Am J Solids Struct.
        2020;17(8): 1–21. https://doi.org/10.1590/1679-78256021

[47]   Topilla L, Toros S. Gurson-Tvergaard-Needleman (GTN) parameters of DP steels with different rolling
        directions were determined and investigated at different strain rates. Eurasian Journal of Science
        Engineering and Technology.;3(2):71-83. https://doi.org/10.55696/ejset.1113577

[48]   Topilla L, Toros S. Stress-strain distribution and failure mechanisms in dual-phase steels investigated
        with microstructure-based modeling. Latin American Journal of Solids and Structures. 2022 Nov 28;19:
        1-21. https://doi.org/10.1590/1679-78257157

Labinot Topilla[*]
University for Business and Technology,
Prishtina, Kosovo

Serkan Toros
Nigde Omer Halisdemir University,
Mechanical Engineering Department,
Nigde, Turkey
[*]Corresponding author:
labinot.topilla@gmail.com